Carbon Matrix with Atomic Dispersion of Binary Cobalt/Iron-N Sites as Efficient Peroxymonosulfate Activator for Organic Pollutant Oxidation.

ZHANG, Bofan, LI, Xianquan, BINGHAM, Paul <http://orcid.org/0000-0001-6017-0798>, AKIYAMA, Kazuhiko and KUBUKI, Shiro

Supporting Information

Carbon Matrix with Atomic Dispersion of Binary Cobalt/Iron-N Sites as Efficient Peroxymonosulfate Activator for Organic Pollutants Oxidation

Bofan Zhang[1, †, *], Xianquan Li[2, †], Paul A. Bingham[3], Kazuhiko Akiyama[1], Shiro Kubuki[1]

[1]Department of Chemistry, Tokyo Metropolitan University, Tokyo 192-0397, Japan

[2]Dalian Institute of Chemical Physics, Chinese Academy of Sciences, Dalian 116023, China

[3]College of Business, Technology and Engineering, Sheffield Hallam University, Howard Street, Sheffield S1 1WB, UK

*Corresponding author: Bofan Zhang

E-mail: 15054218031@163.com (B.F. Zhang)

† These authors contributed equally

S1. Chemicals

$FeCl_3 \cdot 6H_2O$, $Co(NO_3)_2 \cdot 6H_2O$, 1,4-benzenedicarboxylic acid (1,4-BDC), N, N-dimethylformamide (DMF), melamine, methanol (MeOH), tert-Butyl Alcohol (TBA), p-benzoquinone, 1,10-phenanthroline and furfuryl alcohol were purchased from Siyaku Chemical Reagent Co. ,Ltd., Japan. All reagents used were analytical grade reagents.

S2. Characterization

X-ray diffraction (XRD) patterns were obtained from an X-ray diffractometer with Cu Kα radiation, then were applied to evaluate the crystal structure of the samples. The morphology and composition of catalysts were analyzed by scanning electron microscopy and transmission electron microscopy (SEM/TEM, JEM-3200FS) and energy-dispersive X-ray spectroscopy (EDX). The X-ray absorption fine structure spectra were measured on the 1W1B station in Beijing Synchrotron Radiation Facility (BSRF). Data were collected through a fixed-exit double-crystal Si (111) monochromator. The obtained the data were analyzed by Athena and Artemis. Surface electronic states were recorded by X-ray photoelectron spectroscopy (XPS, VG MultiLab 2000). The N_2 adsorption-desorption measurements were analyzed by the nitrogen adsorption apparatus (ASAP 2020, USA). The iron and cobalt concentration were measured using inductively coupled plasma optical emission spectroscopy (ICP-OES). The total organic carbon (TOC) was analyzed using a multi N/C 3100 analyzer. ^{57}Fe Mössbauer spectra of Fe-MOF and FeN_x-C catalysts were obtained using ^{57}Co (Rh) γ–ray radioactive source maintained at room temperature (298 K). EPR spectra were recorded using a Brucker ESR A300-10/12 spectrometer at room temperature. The open-circuit voltage, linear sweep voltammetry (LSV) and electrochemical impedance spectroscopy (EIS) were performed on a CHI 660D electrochemical workstation with a standard three-electrode electrochemical cell (Pt electrode, FTO glass and saturated calomel electrode). Firstly, the

homogeneous catalyst ink was prepared: 5 mg catalyst was dissolved in 250 μL DI and 20 μL Nafion reagent and then ultrasonicated for 30 min. Afterwards, the mixture was dropped onto the FTO glass surface (1 x 1 cm) and dried in ambient environment. Specifically, Nyquist plots were measured under frequency from 10^5 to 10^{-2} Hz at a stable initial voltage. LSV measurement was conducted at potential range of 0V-1V vs Ag/AgCl with a scan rate of 50 mV. Open-circuit voltage was performed in a standard three electrode electrochemical cell. After waiting for the open circuit voltage to stabilize, PMS and BPA were added at an interval of 200 seconds. As for the turnover frequency (TOF) value calculation, the ratio of the molar amount of substrate converted to the molar amount of catalyst used in a reaction in unit time, as shown below:

$$\mathrm{TOF} = \frac{moles\ of\ degraded\ substrate}{mole\ of\ active\ sites\ \times\ reaction\ time}$$

S3. Density functional theory (DFT) calculation

Density functional theory calculations were performed using Vienna Ab Initio Package (VASP) within the generalized gradient approximation (GGA) using the PBE formulation. The projected augmented wave (PAW) potentials to describe the ionic cores and take valence electrons into account using a plane wave basis set with a kinetic energy cutoff of 450 eV. Partial occupancies of the Kohn−Sham orbitals were allowed using the Gaussian smearing method and a width of 0.05 eV. The electronic energy was considered self-consistent when the energy change was smaller than 10−5 eV. A geometry optimization was considered convergent when the force change was smaller than 0.03 eV/Å. Finally, the adsorption energies (E_{ads}) are calculated as $E_{ads}= E_{ad/sub} -E_{ad} -E_{sub}$, where $E_{ad/sub}$, E_{ad} and E_{sub} are the optimized adsorbate/substrate system, the adsorbate in the structure and the clean substrate, respectively.

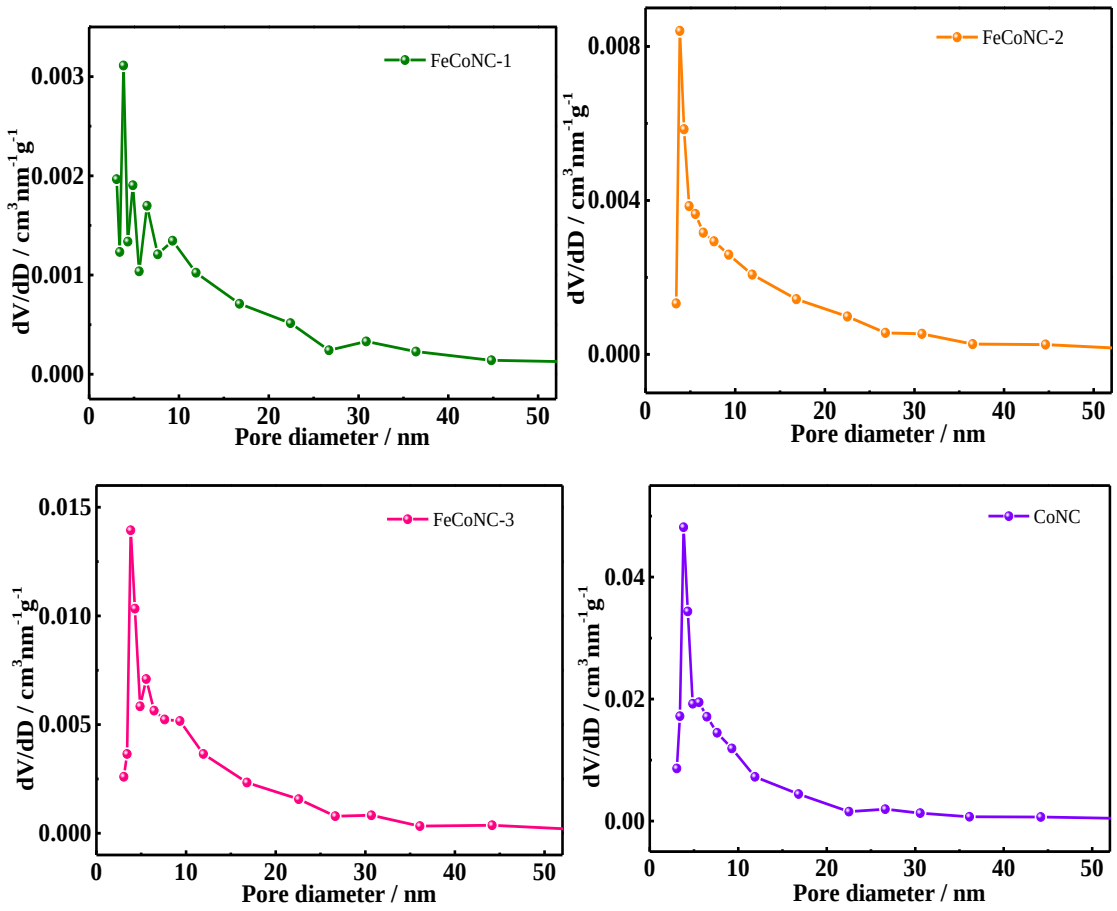

Figure S1. N_2 adsorption-desorption isotherm and pore size distribution of as-synthesized catalysts

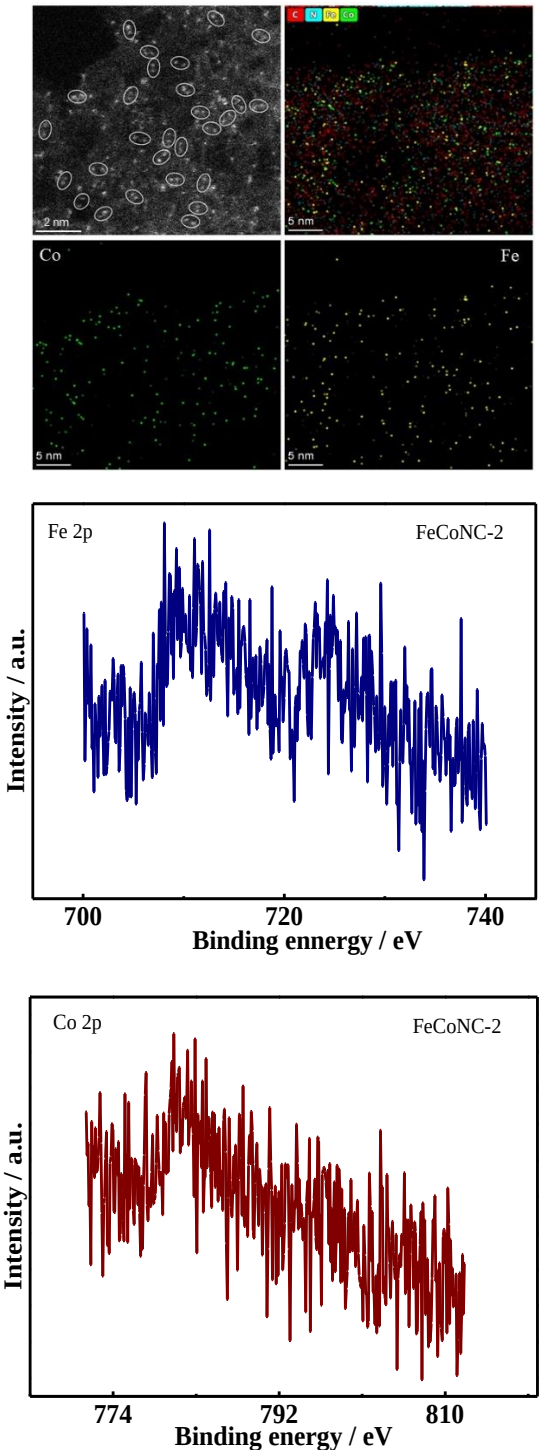

Figure S2. HAADF-STEM image and EDS-mapping images; High resolution XPS spectra of Fe 2p and Co 2P in FeCoNC-2 catalyst

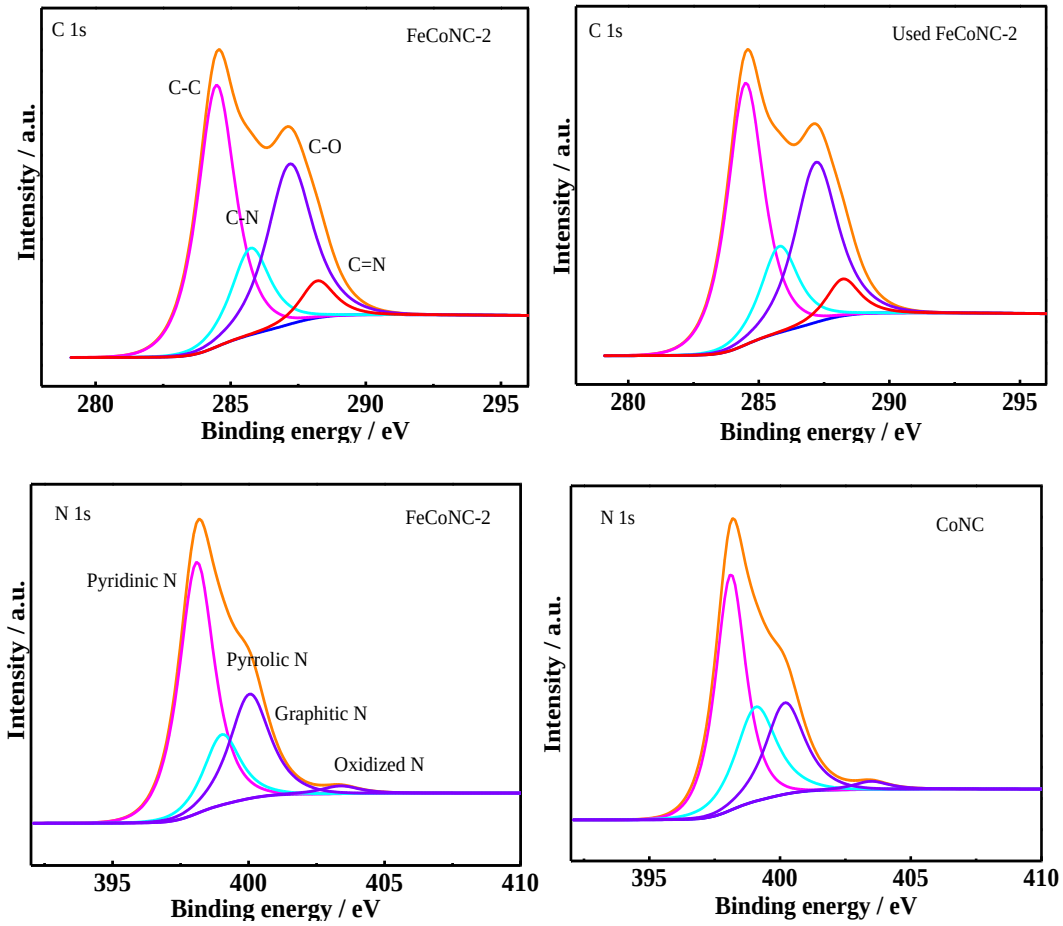

Figure S3. High resolution C 1s XPS spectra of fresh and used FeCoNC-2 catalysts; N 1s XPS spectra of FeCoNC-2 and CoNC catalysts

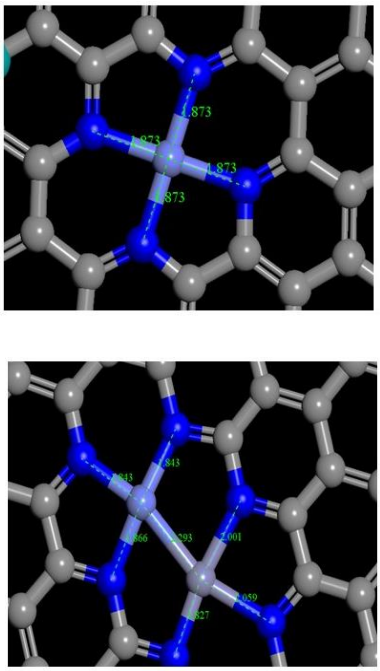

Figure S4. Bond length between Fe, Co and N atoms in CoNC (above) and FeCoNC (below) catalysts

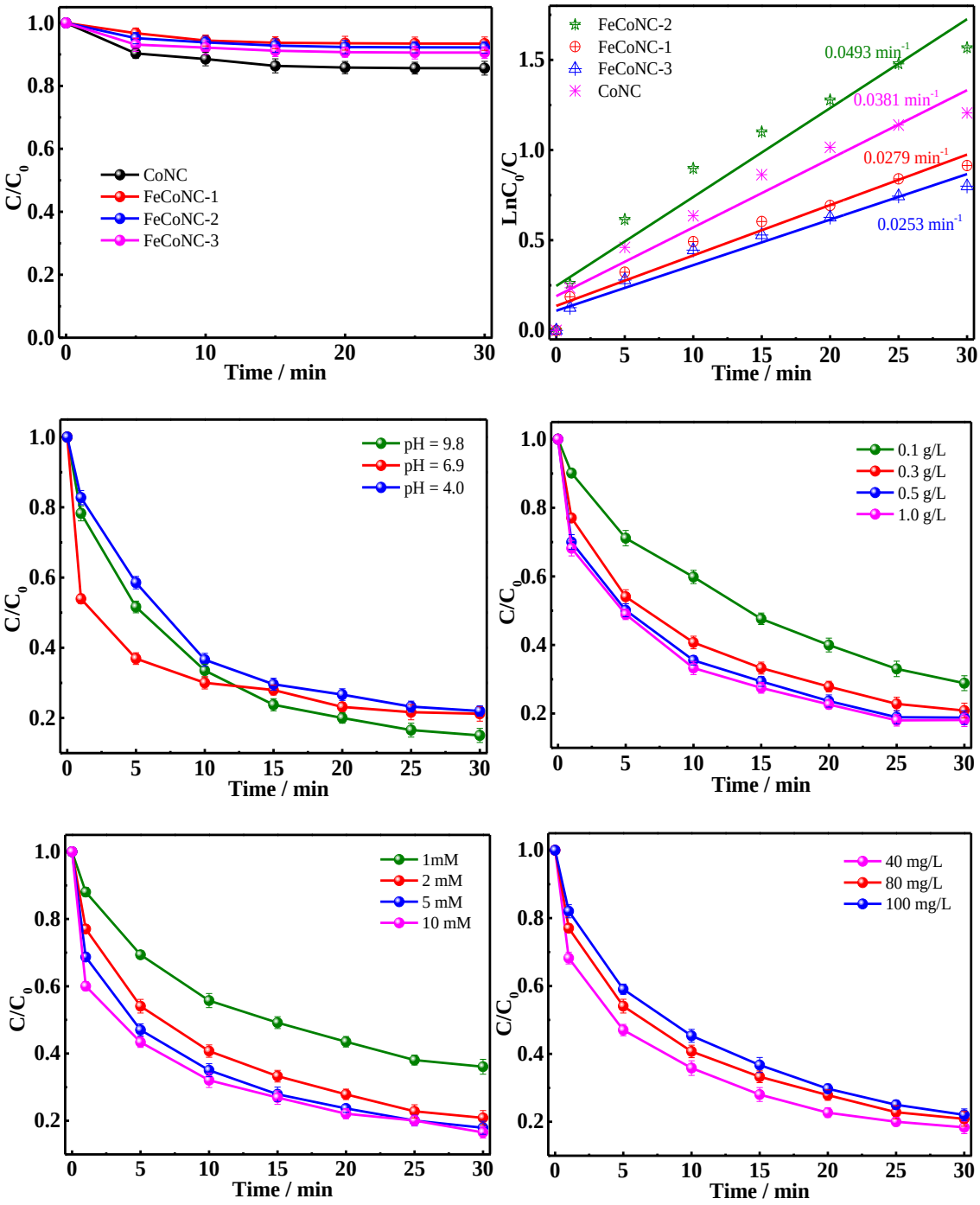

Figure S5. (a) The adsorption ability towards TC via synthesized catalysts; (b) Kinetic curve of TC degradation via synthesized catalysts; TC degradation under different parameters: (c) initial pH value; (d) catalyst dosage; (e) PMS concentration and (f) TC concentration

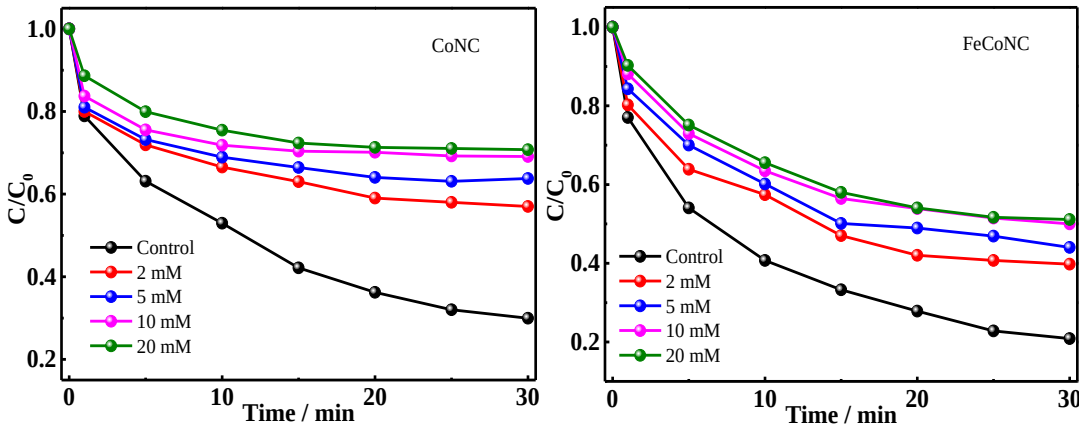

Figure S6. Effect of FFA concentration on TC removal rate in CoNC/PMS and FeCoNC/PMS systems

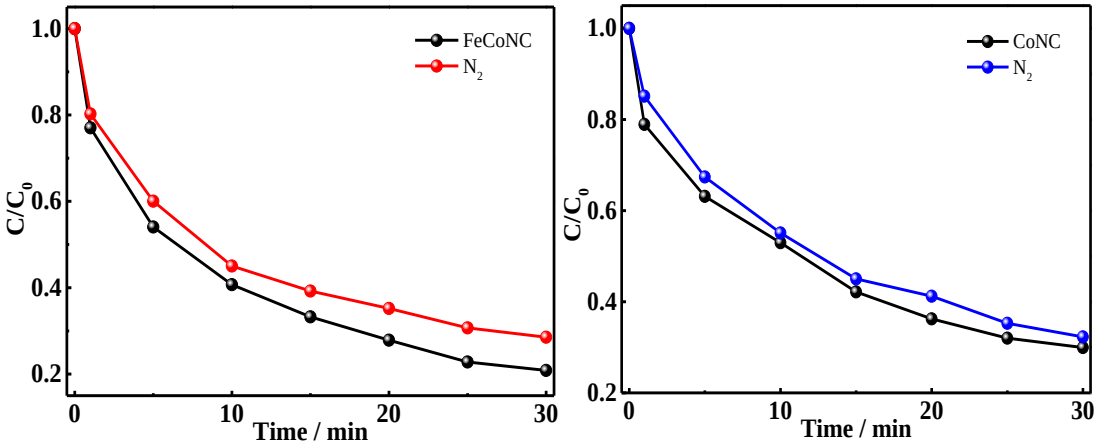

Figure S7. Degradation of TC in the presence or absence of N_2 in FeCoNC and CoNC/PMS system

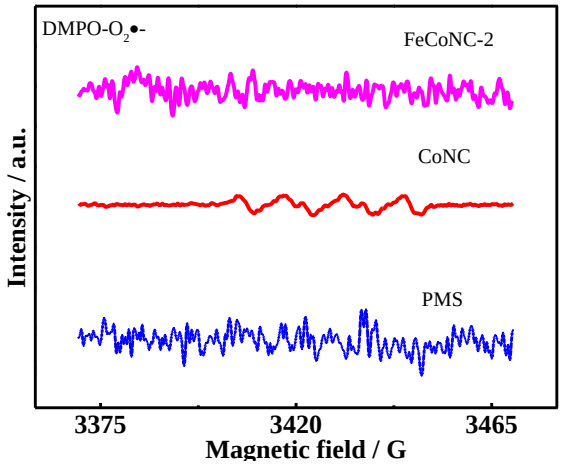

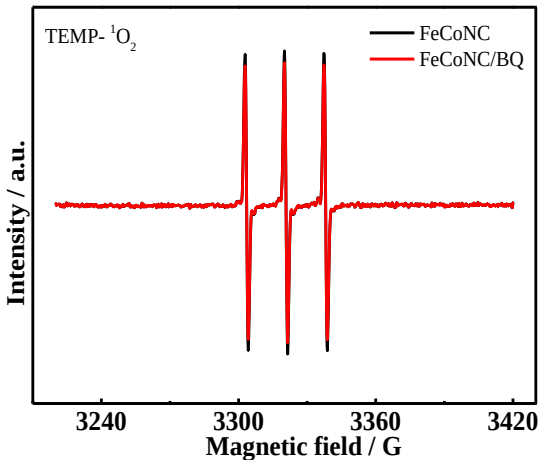

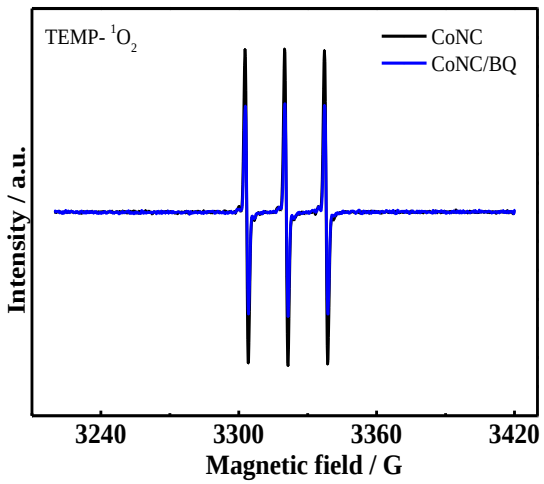

Figure S8. EPR spectra of $^1O_2$ generated by FeCoNC and CoNC in the presence of BQ scavenger

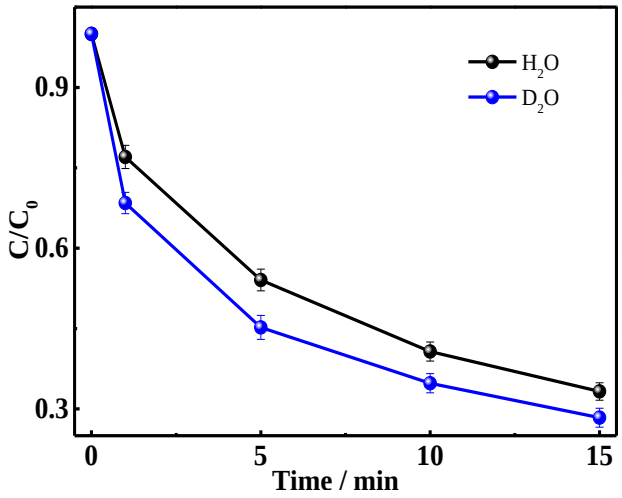

Figure S9. TC degradation efficiency in the FeCoNC/PMS system in the presence of H_2O or D_2O

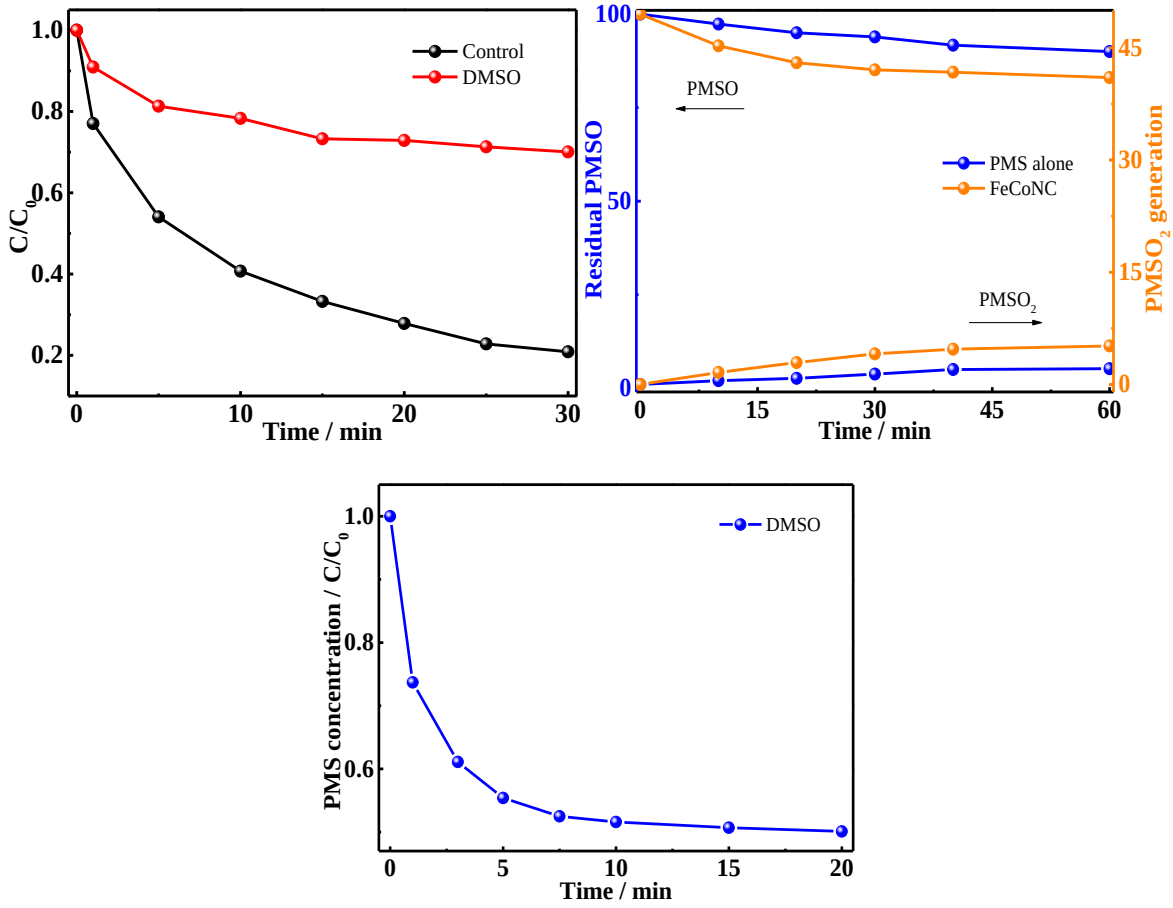

Figure S10. (a) Effect of DMSO scavenger on TC degradation in FeCoNC/PMS system; (b) PMSO consumption and $PMSO_2$ generation in PMS alone and FeCoNC systems; (c) Consumption of PMS by DMSO scavenger

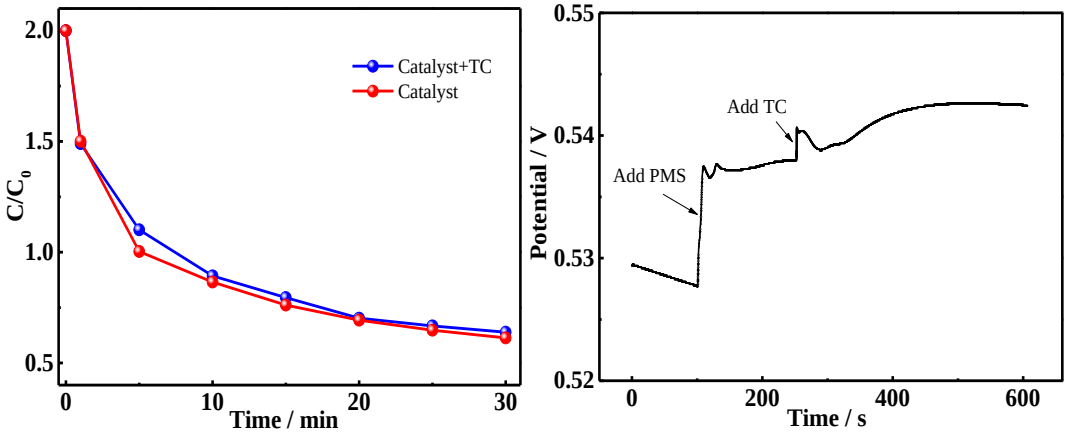

Figure S11 (a) FeCoNC-initiated PMS decomposition; (b) Chronopotentiometry curve with adding PMS and TC solutions

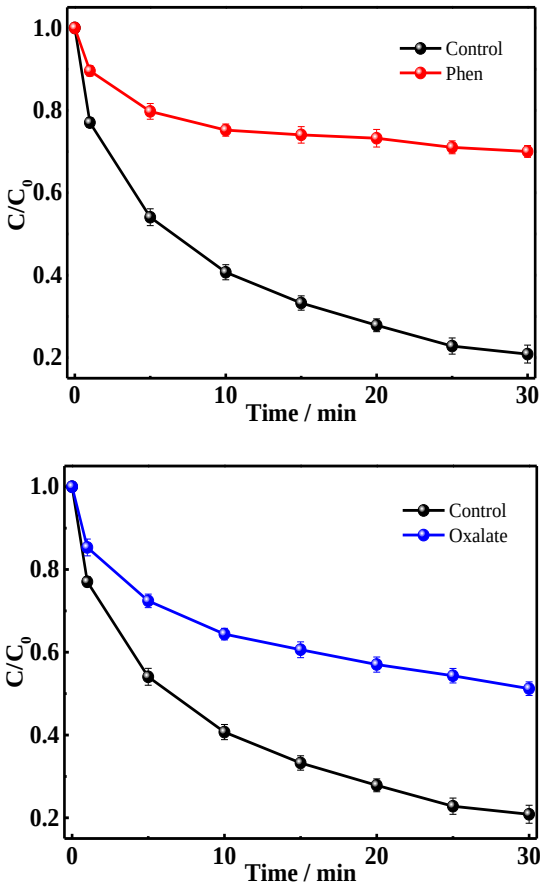

Figure S12. Influence of phenanthroline (Phen) and Oxalate on TC degradation by FeCoNC-2 catalyst

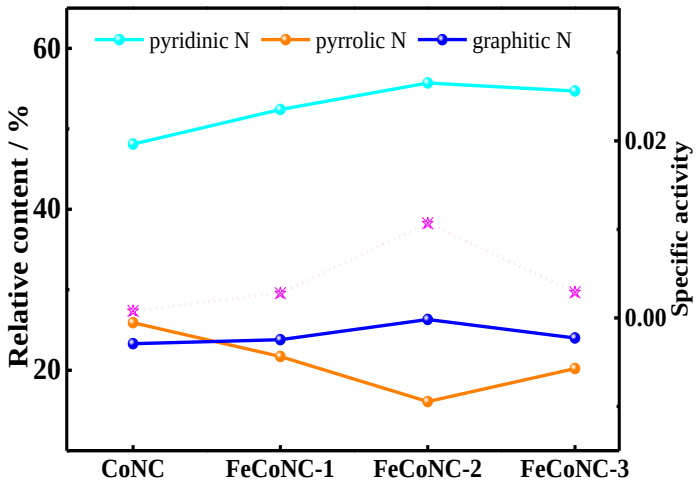

Figure S13. Correlation ship between specific catalytic activity and relative content of N species

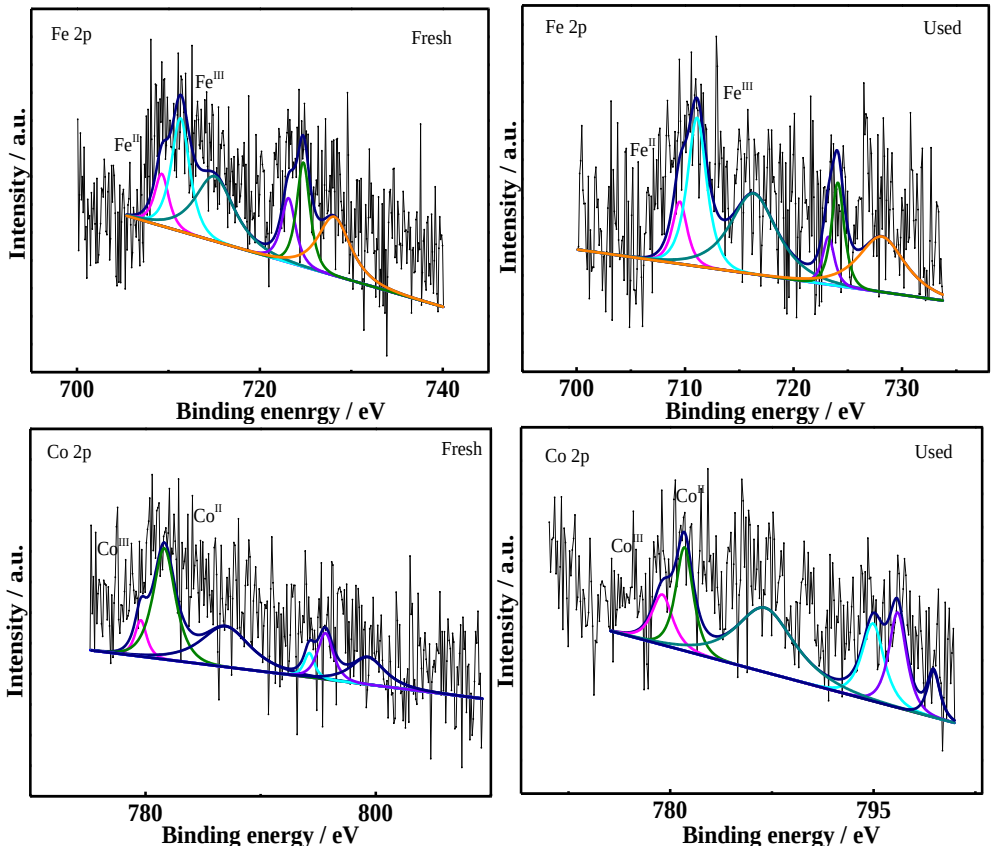

Figure S14. High resolution Fe 2p XPS spectra and Co 2p spectra of FeCoNC-2 catalyst before and after reaction

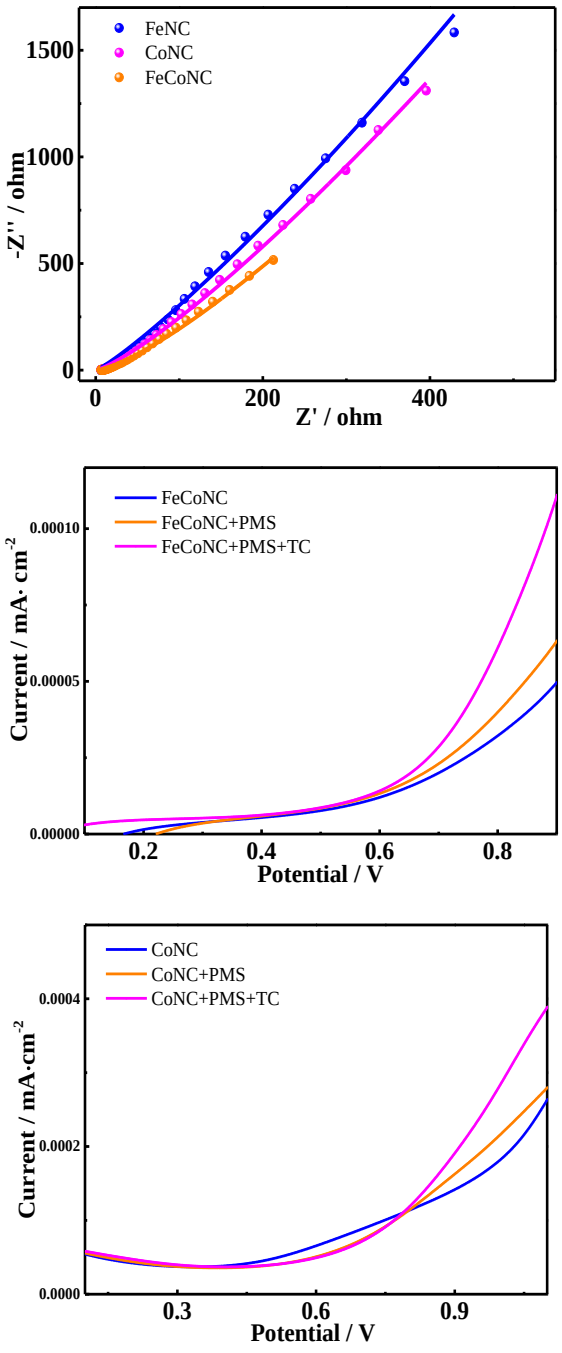

Figure S15. (a) EIS Nyquist plots; (b-c) Linear sweep voltammetry (LSV) curves in different systems

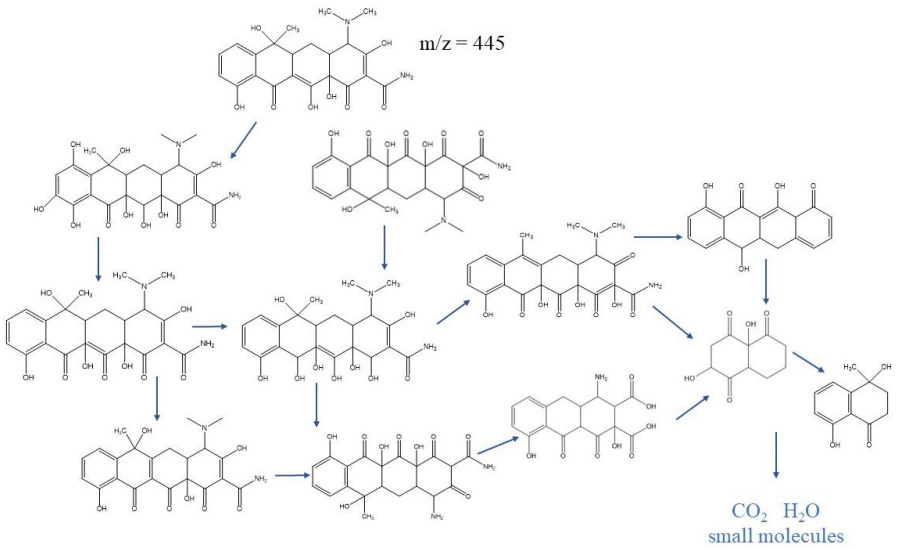

CoNC/PMS system

Figure S16. The possible degradation pathways of TC in CoNC/PMS system

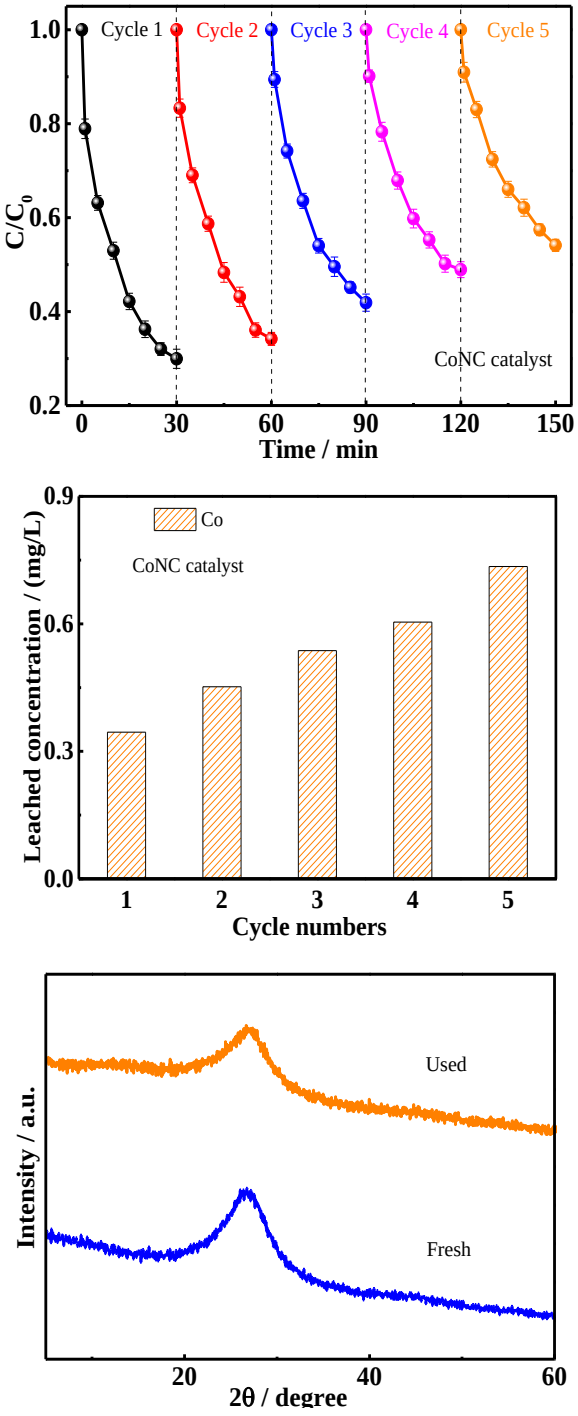

Figure S17. (a) The reusability test of CoNC for TC degradation; (e) Leached metal Co concentration after each cyclic experiment; (c)XRD pattern of fresh and used FeCoNC-2 sample

Table S1. Structural parameters of BET surface area, pore volume and pore size

Catalyst	BET Surface area (m^2/g)	Pore volume (cm^3/g)	Average pore size (nm)
CoNC	116.81	0.238	3.824
FeCoNC-1	29.45	0.060	3.820
FeCoNC-2	15.36	0.032	3.823
FeCoNC-3	43.24	0.100	3.826

Table S2. Normalized *k* value for TC degradation by as-prepared catalysts

Catalyst	*k* value min^{-1}	Normalized *k* value $L\ min^{-1}\ m^{-2}$	Turnover frequency (TOF) value min^{-1}
CoNC	0.0381	0.0010	0.042
FeCoNC-2	0.0493	0.0107	0.105
FeCoNC-3	0.0253	0.0029	0.063
FeCoNC-1	0.0279	0.0023	0.087

Table S3. Elemental content of FeCoNC catalysts before and after PMS activation by XPS analysis

Catalyst	Fe	Co	N	O	C
CoNC	--	0.47	35.54	9.38	54.61
FeCoNC-2	0.39	0.28	38.07	6.56	54.70
FeCoNC-2 after PMS activation	0.35	0.26	32.25	12.58	54.56

Table S4. EXAFS fitting parameters at the Co K–edge for FeCoNC and references sample

Sample	Shell	CN^a	R(Å)^b	σ^2(Å^2)^c	ΔE_0(eV)^d	R factor
Co foil	Co-Co	12*	2.49±0.01	0.0061±0.0003	7.1±0.4	0.0006
CoPc	Co-N	3.9±0.7	1.93±0.02	0.0049±0.0023	8.8±2.2	0.0132
FeCoNC	Co-N	2.9±0.7	1.91±0.04	0.0067±0.0037	6.4±1.0	0.0175
	Co-Fe	0.9±0.4	2.73±0.01	0.0056±0.0032	7.3±1.8	

$^a CN$, coordination number; $^b R$, distance between absorber and backscatter atoms; $^c \sigma^2$, Debye-Waller factor to account for both thermal and structural disorders; $^d \Delta E_0$, inner potential correction; R factor indicates the goodness of the fit. S_0^2 was fixed to 0.71, according to the experimental EXAFS fit of Co foil by fixing CN as the known crystallographic value. A reasonable range of EXAFS fitting parameters: $0.700 < S_0^2 < 1.000$; $CN > 0$; $\sigma^2 > 0$ Å^2; $|\Delta E_0| < 10$ eV; R factor < 0.02.

Table S4. EXAFS fitting parameters at the Fe K–edge for FeCoNC and references sample

Sample	Shell	CN^a	R(Å)^b	σ^2(Å^2)^c	ΔE_0(eV)^d	R factor
Fe foil	Fe-Fe1	8*	2.47±0.07	0.0047±0.0020	5.7±1.4	0.0015
	Fe-Fe2	6*	2.84±0.09	0.0054±0.0043	3.9±2.2	
FePc	Fe-N	4.2±0.9	1.97±0.02	0.0082±0.0020	7.7±1.8	0.0024
Fe sample	Fe-N	3.1±1.2	2.06±0.02	0.0036±0.0027	8.8±2.1	0.0048
	Fe-Co	1.0±0.5	2.75±0.03	0.0093±0.0018	8.0±2.5	

$^a CN$, coordination number; $^b R$, distance between absorber and backscatter atoms; $^c \sigma^2$, Debye-Waller factor to account for both thermal and structural disorders; $^d \Delta E_0$, inner potential correction; R factor indicates the goodness of the fit. S_0^2 was fixed to 0.72, according to the experimental EXAFS fit of Fe foil by fixing CN as the known crystallographic value. A reasonable range of EXAFS fitting parameters: $0.700 < S_0^2 < 1.000$; $CN > 0$; $\sigma^2 > 0$ Å^2; $|\Delta E_0| < 10$ eV; R factor < 0.02.

Table S5. ^{57}Fe Mössbauer parameters and assignment of the components featured in the deconvoluted Mössbauer spectra of FeCoNC catalysts

Catalyst	Component	IS/mms^{-1}	QS/mms^{-1}	Area/%	Assignment
FeCoNC-1	D1	1.250	3.35	20.5	$Fe^{II}N_x$
	D2	0.437	0.98	79.5	$Fe^{III}N_x$
FeCoNC-2	D1	1.258	3.21	15.1	$Fe^{II}N_x$
	D2	0.401	0.838	84.9	$Fe^{III}N_x$
FeCoNC-3	D1	1.099	3.19	21.2	$Fe^{II}N_x$
	D2	0.409	0.99	78.8	$Fe^{III}N_x$
Used FeCoNC-2	D1	1.255	3.45	10.5	$Fe^{II}N_x$
	D2	0.401	0.92	89.5	$Fe^{III}N_x$

Table S6. Comparison of catalytic reactivity of FeCoNC catalyst with previous reported catalysts during PMS activation

Catalyst	Catalyst dosage ($g\ L^{-1}$)	TC concentration ($mg\ L^{-1}$)	PMS (mM)	Degradation time (min)	Removal rate (%)	Rate constant (min^{-1})	Ref.
CA-900	0.2	10	2.0	90	90	0.0096	1[1]
R-N-Fe	0.5	100	2.0	275	80	--	2[2]
Co-MIL-53(Al)	0.3	30	2.0	120	90	0.0310	3[3]
Co-PPCC	1.0	50	1.0	60	90	--	4[4]
PFSC-900	0.4	20	1.0	120	90	0.0317	5[5]
Rice husk biochar	4.0	20	20	120	90	--	6[6]
FeS_2	2.0	50	1.0	120	89	0.0099	7[7]
MIL-125(Ti)-NH_2-Fe	0.1	20	4.5	40	90	0.0355	8[8]
AC@Fe_3O_4	0.2	30	PS/30	180	80.7	0.0098	9[9]
BC/CN-15	0.2	10	1.0	60	89	0.0351	10[10]
FeCo/N-C	0.3	80	2.0	30	82	0.0493	This work

Reference

[1] H. Yang, Z. Ding, Y. Liu, S. Zhang, Y. Zou, G. Bai, Y. Zhang, S. Xia, Biomass-derived carbon aerogel for peroxymonosulfate activation to remove tetracycline: Carbonization temperature, oxygen-containing functional group content, and defect degree, Ind. Crops Prod., 177 (2022) 114437.

[2] Y. Sun, W. Zheng, S. Fu, R.P. Singh, Immobilization of iron phthalocyanine on 4-aminopyridine grafted polystyrene resin as a catalyst for peroxymonosulfate activation in eliminating tetracycline hydrochloride, Chem. Eng. J., 391 (2020) 123611.

[3] F. Liu, J. Cao, Z. Yang, W. Xiong, Z. Xu, P. Song, M. Jia, S. Sun, Y. Zhang, X. Zhong, Heterogeneous activation of peroxymonosulfate by cobalt-doped MIL-53(Al) for efficient tetracycline degradation in water: Coexistence of radical and non-radical reactions, J. Colloid Interface Sci., 581 (2021) 195-204.

[4] S. Han, P. Xiao, L. An, D. Wu, Oxidative degradation of tetracycline using peroxymonosulfate activated by cobalt-doped pomelo peel carbon composite, Environ. Sci. Pollut. Res., 29 (2022) 21656-21669.

[5] Y. Hu, D. Chen, R. Zhang, Y. Ding, Z. Ren, M. Fu, X. Cao, G. Zeng, Singlet oxygen-dominated activation of peroxymonosulfate by passion fruit shell derived biochar for catalytic degradation of tetracycline through a non-radical oxidation pathway, J. Hazard. Mater., 419 (2021) 126495.

[6] P.T. Huong, K. Jitae, T.M. Al Tahtamouni, N. Le Minh Tri, H.-H. Kim, K.H. Cho, C. Lee, Novel activation of peroxymonosulfate by biochar derived from rice husk toward oxidation of organic contaminants in wastewater, J. Water Process Eng., 33 (2020) 101037.

[7] X. Chen, N. Zhao, X. Hu, A novel strategy of pulsed electro-assisted pyrite activation of peroxymonosulfate for the degradation of tetracycline hydrochloride, Sep. Purif. Technol., 280

(2022) 119781.

[8] Y. Fan, W. Zhang, K. He, L. Wang, Q. Wang, J. Liu, Half-salen Fe(III) covalently post-modified MIL-125(Ti)-NH_2 MOF for effective photocatalytic peroxymonosulfate activation, Appl. Surf. Sci., 591 (2022) 153115.

[9] A. Jonidi Jafari, B. Kakavandi, N. Jaafarzadeh, R. Rezaei Kalantary, M. Ahmadi, A. Akbar Babaei, Fenton-like catalytic oxidation of tetracycline by AC@Fe_3O_4 as a heterogeneous persulfate activator: Adsorption and degradation studies, J. Ind. Eng. Chem., 45 (2017) 323-333.

[10] R. Tang, D. Gong, Y. Deng, S. Xiong, J. Zheng, L. Li, Z. Zhou, L. Su, J. Zhao, π-π stacking derived from graphene-like biochar/g-C_3N_4 with tunable band structure for photocatalytic antibiotics degradation via peroxymonosulfate activation, J. Hazard. Mater., 423 (2022) 126944.